

# Crystallization of bosonic quantum Hall states in a rotating quantum gas

<https://doi.org/10.1038/s41586-021-04170-2>

Received: 21 June 2021

Accepted: 21 October 2021

Published online: 5 January 2022

 Check for updates

Biswaroop Mukherjee<sup>1</sup>, Airlia Shaffer<sup>1</sup>, Parth B. Patel<sup>1</sup>, Zhenjie Yan<sup>1</sup>, Cedric C. Wilson<sup>1</sup>, Valentin Crépel<sup>1</sup>, Richard J. Fletcher<sup>1</sup> & Martin Zwierlein<sup>1✉</sup>

The dominance of interactions over kinetic energy lies at the heart of strongly correlated quantum matter, from fractional quantum Hall liquids<sup>1</sup>, to atoms in optical lattices<sup>2</sup> and twisted bilayer graphene<sup>3</sup>. Crystalline phases often compete with correlated quantum liquids, and transitions between them occur when the energy cost of forming a density wave approaches zero. A prime example occurs for electrons in high-strength magnetic fields, where the instability of quantum Hall liquids towards a Wigner crystal<sup>4–9</sup> is heralded by a roton-like softening of density modulations at the magnetic length<sup>7,10–12</sup>. Remarkably, interacting bosons in a gauge field are also expected to form analogous liquid and crystalline states<sup>13–21</sup>. However, combining interactions with strong synthetic magnetic fields has been a challenge for experiments on bosonic quantum gases<sup>18,21</sup>. Here we study the purely interaction-driven dynamics of a Landau gauge Bose–Einstein condensate<sup>22</sup> in and near the lowest Landau level. We observe a spontaneous crystallization driven by condensation of magneto-rotons<sup>7,10</sup>, excitations visible as density modulations at the magnetic length. Increasing the cloud density smoothly connects this behaviour to a quantum version of the Kelvin–Helmholtz hydrodynamic instability, driven by the sheared internal flow profile of the rapidly rotating condensate. At long times the condensate self-organizes into a persistent array of droplets separated by vortex streets, which are stabilized by a balance of interactions and effective magnetic forces.

When electrons are placed in a magnetic field, their kinetic energy is quenched. The single particle states form discrete, highly degenerate Landau levels, and correspond to wavepackets localized to the magnetic length  $\ell_B$ . In the presence of interactions between electrons, owing to the absence of kinetic energy, one naturally expects the formation of a Wigner crystal of periodicity  $\sim \ell_B$  (refs. <sup>4–6,8,9,23</sup>). Famously, however, the interplay of the macroscopic degeneracy and interactions instead typically favours the strongly correlated fractional quantum Hall liquids, which host fractional charges, anyonic exchange statistics and topologically protected transport properties<sup>1</sup>. The tendency to crystallize is still apparent in a pronounced minimum in the collective excitation spectrum at wavevectors  $k \sim 1/\ell_B$  (refs. <sup>7,10–12</sup>). In analogy with the roton minimum in <sup>4</sup>He, also considered a precursor of solidification<sup>24</sup>, these excitations are called magneto-rotons<sup>7,11,12</sup>.

The fate of interacting bosons in the presence of a gauge field is of fundamental importance in the classification of topological states of matter<sup>19</sup>. Quantum Hall states<sup>13,16,20</sup>, exotic vortex lattices<sup>14</sup> and vortex-free states under extreme fields<sup>17</sup> were predicted. Quantum phase transitions between such states were found to be signalled by the softening of a roton-like collective mode<sup>15,25</sup>.

Bosonic quantum gases in artificial magnetic fields<sup>18,21</sup> have been generated via spin–orbit coupling<sup>21,26,27</sup>, phase imprinting in lattices<sup>28–32</sup> and by rotation of the trapped gas<sup>16,22,33,34</sup>. The latter approaches the analogy between the Lorentz force on a charged particle in a magnetic field, and the Coriolis force on a massive particle in a frame rotating at

frequency  $\Omega$ , giving  $\omega_c = 2\Omega$  and  $\ell_B = \sqrt{\hbar/(m\omega_c)}$  as the rotational analogue of the cyclotron frequency and the magnetic length, respectively.

Signatures of physics near the lowest Landau level (LLL) have been observed in rotating Bose gases<sup>33,34</sup>. In recent work at MIT, condensates have been prepared directly in the lowest Landau gauge wavefunction using geometric squeezing<sup>22</sup>. In this mean-field quantum Hall regime<sup>13</sup>, all bosons occupy a single wavefunction, whose subsequent dynamics subject to a gauge field can be studied, offering a microscopic insight into the individual building blocks of quantum Hall systems. An advantage of rotation is that the interactions between atoms are decoupled from the induced gauge potential, in contrast to other methods for which the effective magnetic field appears within a dressed-atom picture, leading to additional unwanted interaction terms<sup>35</sup>.

Here we directly observe the evolution of an interacting Bose–Einstein condensate occupying a single Landau gauge wavefunction in the LLL. We find that the Landau gauge condensate is unstable under the influence of interactions, exhibiting spontaneous growth of a snaking mode leading to a persistent density wave order at the magnetic length  $\ell_B$  as illustrated in Fig. 1. At the heart of this crystallization is the coupling between the relative momentum and spatial overlap of two particles in a gauge field. This lowers the interaction energy cost of populating higher-momentum states, and leads to the dynamical instability of the lowest (Goldstone) collective excitation branch<sup>15</sup> (see Supplementary Information). The ensuing proliferation of excitations at momenta near

<sup>1</sup>MIT-Harvard Center for Ultracold Atoms, Research Laboratory of Electronics, Department of Physics, Massachusetts Institute of Technology, Cambridge, MA, USA. ✉e-mail: [zwierlei@mit.edu](mailto:zwierlei@mit.edu)

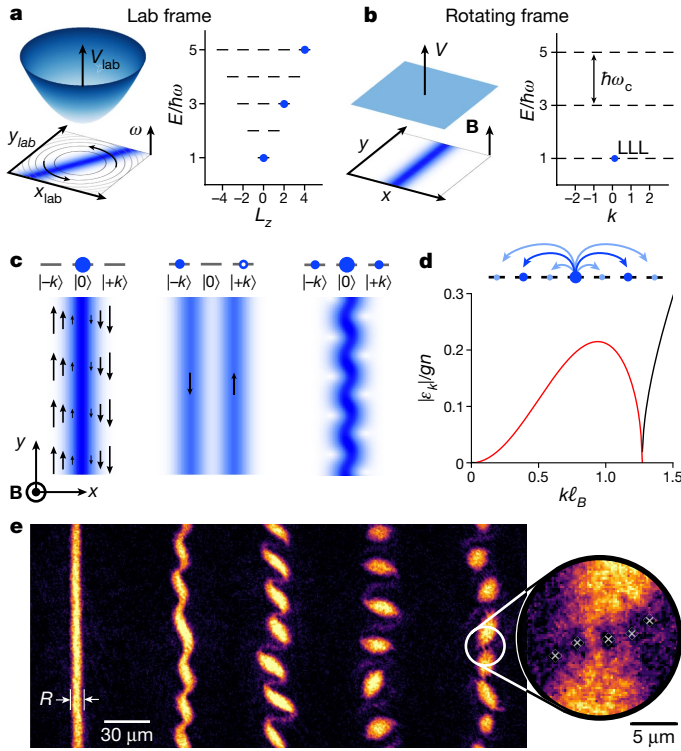


**Fig. 1 | Spontaneous crystallization of an interacting Bose-Einstein condensate in an artificial magnetic field.** **a**, In the laboratory frame, the condensate freely rotates in a circularly symmetric harmonic trap at the trapping frequency  $\omega$ . Occupied states in the energy spectrum are sketched ( $L_z$ , angular momentum). **b**, In the rotating frame, the condensate experiences an effective magnetic field  $B$  but no scalar potential. The energy spectrum is flattened into Landau levels ( $k$ , momentum along  $y$ ). Only the  $k = 0$  Landau gauge wavefunction is occupied. **c**, The irrotationality of the condensate in the laboratory frame imposes a sheared velocity profile in the rotating frame, which is dynamically unstable towards a periodic density modulation. Motion with momentum  $\hbar k$  along the  $y$ -direction is tied to sideways displacement of the wavefunction along  $x$ . The reduced overlap of  $|k| > 0$  states with the  $k = 0$  condensate lowers the interaction energy cost of collective excitations, leading to spontaneous population of  $\pm k$  pairs whose interference with the condensate results in a density modulation. **d**, This dynamical instability is reflected in a (Goldstone) collective excitation branch, which is imaginary across a range of wavevectors, shown by a red line. The spectrum shown is calculated for a condensate in the LLL, for which the interaction energy  $gn$  provides the only relevant energy scale and the magnetic length  $\ell_B = 1.6 \mu\text{m}$  sets the lengthscale. Here  $g$  is the mean-field coupling constant, and  $n = n_{2D}(0)$  is the peak two-dimensional density. **e**, Absorption images of the evolution of the condensate density in the rotating frame, displaying a snake-like instability and the formation of droplet arrays. Here the cloud width is  $R = 2.34\ell_B$ , and the frames are taken at 0, 5, 6.2, 8.5 and 10 cyclotron periods ( $2\pi/\omega_c = 5.6 \text{ ms}$ ). The magnification reveals vortex streets between adjacent droplets (grey crosses), indicating counterflow at their interface.

$\hbar/\ell_B$  can be viewed as condensation of magneto-rotons, in analogy with the Wigner crystal instability of quantum Hall systems<sup>4–9</sup>.

Condensation at non-zero momentum has been predicted in superfluid helium above a critical velocity<sup>36–38</sup>. Roton-like excitations and instabilities in Bose-Einstein condensates have been induced via cavity-mediated interactions<sup>39,40</sup>, spin-orbit coupling<sup>41,42</sup>, shaken optical lattices<sup>43,44</sup>, driven interactions<sup>45</sup> and dipolar interactions<sup>46–48</sup>. These instabilities are tightly connected to evidence for supersolidity, the simultaneous existence of spatial and superfluid order<sup>38,40,42,49–51</sup>. In our case, the instability of density-wave order arises purely from the interplay of contact interactions and a gauge field. No external

drive is present, nor is there any residual scalar potential in the rotating frame. The absence of kinetic energy in the LLL directly implies that the crystallization rate is set solely by the interaction energy of the gas.

By increasing the condensate density such that many Landau levels become populated, we observe a crossover from LLL behaviour to a hydrodynamic instability driven by the sheared internal velocity profile. Analogous phenomena are ubiquitous throughout hydrodynamics, from the diocotron instability in charged plasmas<sup>52</sup> and fragmentation of electron beams<sup>53</sup>, to the Kelvin-Helmholtz instability in atmospheric and astrophysical systems<sup>54,55</sup>. In the context of superfluids, for which the circulation is quantized, the Kelvin-Helmholtz instability has been detected in liquid helium<sup>56</sup>, and theoretically predicted at the boundary between counterflowing condensates<sup>57</sup>. In our superfluid hydrodynamic setting, we directly observe streets of quantized vortices separating emergent droplets, revealing the quantum nature of the instability at the most microscopic level.

To analyse the instability, consider the condensate in the frame rotating at the frequency  $\omega$  of the isotropic harmonic trap, where it experiences a synthetic magnetic field but no scalar potential (see Fig. 1a, b), and thus evolves under the Hamiltonian

$$\hat{H} = \int d^2r \hat{\psi}^\dagger \left[ \frac{(\hat{\mathbf{p}} - q\mathbf{A})^2}{2m} + \frac{g}{2} \hat{\psi}^\dagger \hat{\psi} \right] \hat{\psi}. \quad (1)$$

Here  $\hat{\psi}^\dagger(\mathbf{r})$  is the bosonic field operator,  $\hat{\mathbf{p}}$  is the canonical momentum,  $q$  and  $\mathbf{A}$  are the charge and vector potential in the equivalent magnetic problem, and  $g$  is the two-dimensional mean-field coupling constant. Geometric squeezing prepares a translationally invariant condensate most conveniently described within the Landau gauge  $q\mathbf{A} = (0, m\omega_c x)$  (ref. 22) for which the Hamiltonian becomes

$$\hat{H} = \int d^2r \hat{\psi}^\dagger \left[ \frac{\hat{p}_x^2}{2m} + \frac{1}{2} m \omega_c^2 \left( \hat{x} - \frac{\hat{p}_y \ell_B^2}{\hbar} \right)^2 + \frac{g}{2} \hat{\psi}^\dagger \hat{\psi} \right] \hat{\psi}. \quad (2)$$

Cyclotron motion of the atoms is reflected in an effective harmonic oscillator along the  $x$ -direction of frequency  $\omega_c = 2\omega$ , the non-interacting energy states of which correspond to different Landau levels (see Fig. 1b). Each level is macroscopically degenerate since it costs no energy to translate the centres of cyclotron orbits. Initially, the  $y$  momentum of all atoms is zero, and their cyclotron motion is centred at  $x = 0$  with a two-dimensional number density  $n_{2D}(x)$ . The condensate has uniform phase and thus features a sheared velocity profile  $\mathbf{v} = -q\mathbf{A}/m = (0, -\omega_c x)$  proportional to the vector potential (see Fig. 1c). We parameterize the crossover from LLL to hydrodynamic behaviour by the ratio  $\frac{gn}{\hbar\omega_c}$ , the condensate's mean-field energy of  $\sim gn$  to the Landau level spacing  $\hbar\omega_c$ , giving a measure for the number of occupied Landau levels<sup>22,33</sup>. Here  $n = n_{2D}(0)$  is the peak density. In our experiment  $\frac{gn}{\hbar\omega_c}$  varies from 0.6 to 7.3, corresponding to a central filling fraction  $n\ell_B^2$  of 50 and higher, meaning the condensate lies within the mean-field quantum Hall regime<sup>13,16</sup>.

The dynamical instability illustrated in Fig. 1 can be understood in the low- and high-density limits as follows. When  $gn \lesssim \hbar\omega_c$ , the condensate is restricted to the LLL and shows a Gaussian transverse density profile with a  $1/e$  radius of  $\ell_B$  (ref. 22; see Supplementary Information). A Bogoliubov analysis around this state generically results in a Hamiltonian of the form<sup>15</sup>

$$\hat{H}_{\text{LLL}} = \sum_{k>0} A_k (\hat{a}_k^\dagger \hat{a}_k + \hat{a}_{-k}^\dagger \hat{a}_{-k}) + B_k (\hat{a}_k^\dagger \hat{a}_{-k}^\dagger + \hat{a}_k \hat{a}_{-k}), \quad (3)$$

where  $\hat{a}_k$  is the annihilation operator for a particle with momentum  $\hbar k$  along the  $y$ -direction. This Hamiltonian describes pairs of modes  $\pm k$  with natural frequency  $A_k/\hbar$  and coupled by a pair-creation operator of strength  $B_k$ , which corresponds to a two-mode squeezing interaction

in the language of quantum optics. In a non-rotating uniform condensate,  $A_k = \frac{\hbar^2 k^2}{2m} + gn$  and  $B_k = gn$  (ref. 58), and hence pair creation is always weaker than the mode energy, leading to stable excitations. However, the effective magnetic field profoundly changes this picture. First, in the LLL there is no kinetic energy contribution to  $A_k$ . Second, as illustrated in Fig. 1c, the coupling between momentum and position means that states with  $k \neq 0$  have a reduced overlap with the condensate and a correspondingly lower interaction energy. One finds<sup>15</sup>  $A_k = gn[2\exp(-k^2 \ell_B^2/2) - 1]/\sqrt{2}$  and  $B_k = gn \exp(-k^2 \ell_B^2)/\sqrt{2}$ , and the resulting dispersion  $\varepsilon_k = \sqrt{|A_k|^2 - |B_k|^2}$  is shown in Fig. 1d. The spectrum is imaginary for an entire range of wavevectors  $k > 0$  beyond the zero-energy Goldstone mode at  $k = 0$ , indicating dynamical instability of the Goldstone branch and correlated exponential growth of  $\pm k$  pairs of these modes. Their interference with the  $k = 0$  condensate results in a density modulation (see Fig. 1c). The fastest growth occurs at a wavevector  $-1/\ell_B$  giving a spatial modulation wavelength  $2\pi$  times the magnetic length. This mode eventually becomes macroscopically occupied, corresponding to condensation of magneto-rotons and yielding a density modulation contrast of order unity. Crucially, since interactions provide the only energy scale in the LLL, the instability growth rate is determined purely by the interaction energy  $gn$ .

In the high-density limit where  $gn \gg \hbar\omega_c$ , a hydrodynamic description that neglects quantum pressure is valid. In this regime, the condensate initially exhibits a Thomas–Fermi density profile  $n_{2D} \propto 1 - x^2/R_{TF}^2$  where  $R_{TF} = \sqrt{\frac{2gn}{m\omega_c^2}} = \sqrt{\frac{2gn}{m\omega_c}} \ell_B$  (ref. 59; see Supplementary Information).

The Coriolis force  $2m\mathbf{v} \times \boldsymbol{\Omega}$  on each fluid element resulting from the shear flow  $\mathbf{v} = (0, -\omega_c x)$  perfectly balances the local gradient of mean-field energy, resulting in an inhomogeneous equilibrium density despite the absence of any scalar potential. Our hydrodynamic stability analysis about this equilibrium state reveals a dynamical snaking instability of the cloud (see Supplementary Information), in analogy with the Kelvin–Helmholtz instability of counterflow in fluid layers<sup>54,55</sup>, and the diocotron instability of charged plasmas and electron beams<sup>52,53</sup>. The absence of quantum pressure means that the Thomas–Fermi radius and cyclotron frequency provide the only lengthscale and rate. Within the hydrodynamic analysis the instability develops at a wavevector set by the condensate width, as in the LLL, but at a density-independent rate proportional to  $\omega_c$ , in striking qualitative contrast to the growth rate in the LLL.

From these arguments, for all condensate densities we anticipate an emergent density modulation with a lengthscale set by the width of the initial cloud. For a quantitative analysis, from our experimental images (see Fig. 1e) we obtain the static structure factor  $S_k \equiv |n_k|^2/N$ , where  $n_k = \int dy n_{1D}(y) e^{-iky}$  is the Fourier transform of the one-dimensional number density  $n_{1D}(y)$  and  $N = \int dy n_{1D}(y)$  (ref. 47). In Fig. 2a we show examples of  $S_k$  obtained once the density modulation has fully developed, which show a well defined peak at a wavevector  $k_{max}$ . We attribute the much smaller secondary peak at  $2k_{max}$  to the contiguous traces of condensate linking adjacent droplets. In Fig. 2c we show  $k_{max}$  as a function of the condensate density, which is parameterized by the ratio  $R/\ell_B$  where  $R$  is the full-width at half-maximum of the initial cloud divided by  $2\sqrt{\log 2}$ . This normalization is chosen such that  $R/\ell_B \rightarrow 1$  for vanishing  $gn$ , and in the high-density limit  $R/\ell_B = \sqrt{gn/(\hbar\omega_c \log 2)}$ . At all densities, we indeed find an instability lengthscale of order the cloud width,  $k_{max} \sim 1/R$ . The star indicates the LLL prediction  $k_{max} = 0.98/\ell_B$  and the dashed line shows the hydrodynamic result  $k_{max} = 0.95/R$  neglecting quantum pressure (see Supplementary Information). The solid line presents  $k_{max}$  that we obtain from a numerical solution of the Bogoliubov equations (see Supplementary Information) showing excellent agreement with the data without any free parameters.

Although the cloud width sets the instability lengthscale in both the LLL and hydrodynamic regimes, the growth rate shows qualitatively different behaviour. In Fig. 3a, we show  $S_k$  as a function of time for several

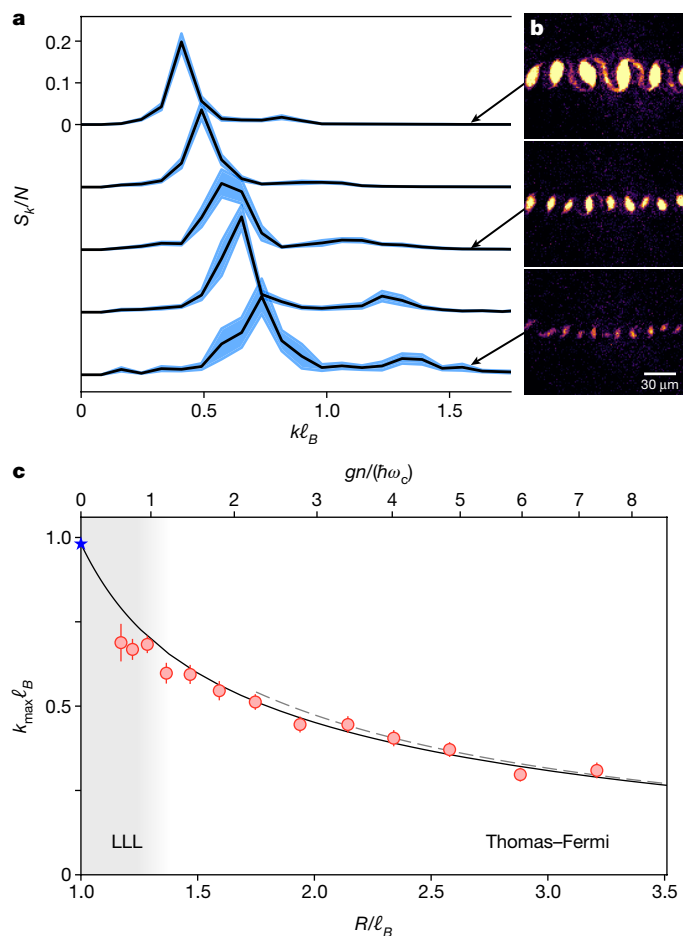


**Fig. 2 | Structure factor and lengthscale of the emergent crystal. a**, The static structure factor,  $S_k$ , measured once the density modulation has reached steady state for condensates with initial widths  $R/\ell_B = 2.58, 1.75, 1.59, 1.28$  and  $1.22$  (top to bottom). The prominent peak reflects the periodic modulation of the cloud density. **b**, Corresponding images of the steady-state crystal, illustrating the decrease in the modulation lengthscale with falling condensate density. **c**, Dependence of the dominant modulation wavevector,  $k_{max}$ , on the cloud width,  $R/\ell_B$ . The LLL and hydrodynamic results are indicated by the star and dashed line, respectively (see text). The solid line shows the prediction of our Bogoliubov analysis (see Supplementary Information), which shows excellent agreement with our data with no free parameters.

different condensate densities. In addition to the decrease in the instability lengthscale at lower densities, we observe a concurrent reduction of the growth rate. At each wavevector we fit the time evolution of the structure factor with the theoretically expected function  $S_k(t) = A \cosh(2\Gamma t)$  (see Supplementary Information), and extract the instability growth rate  $\Gamma(k)$ . This is reported in Fig. 3b, along with the imaginary component of the corresponding Bogoliubov spectrum, which shows good agreement without any free parameters. We note that the experimental data also reveal some growth in  $S_k$  at higher wavevectors than the unstable region predicted by the linear Bogoliubov analysis. We attribute this to nonlinear effects, and have performed numerical simulations of the Gross–Pitaevskii equation, finding that these exhibit the same behaviour (see Supplementary Information).

We capture the typical crystallization rate corresponding to a particular condensate density by the growth rate of the dominant instability,  $\Gamma(k_{max})$ , and in Fig. 3c plot this as a function of  $R/\ell_B$ . When  $R/\ell_B \gg 1$  the rate is density-independent and consistent with our hydrodynamic result  $\Gamma = 0.14\omega_c$ , shown by the dashed line. However, for lower interaction energies the gas enters the LLL where  $gn$  provides the only energy scale. We observe a concurrent slowing down of the instability, and the data



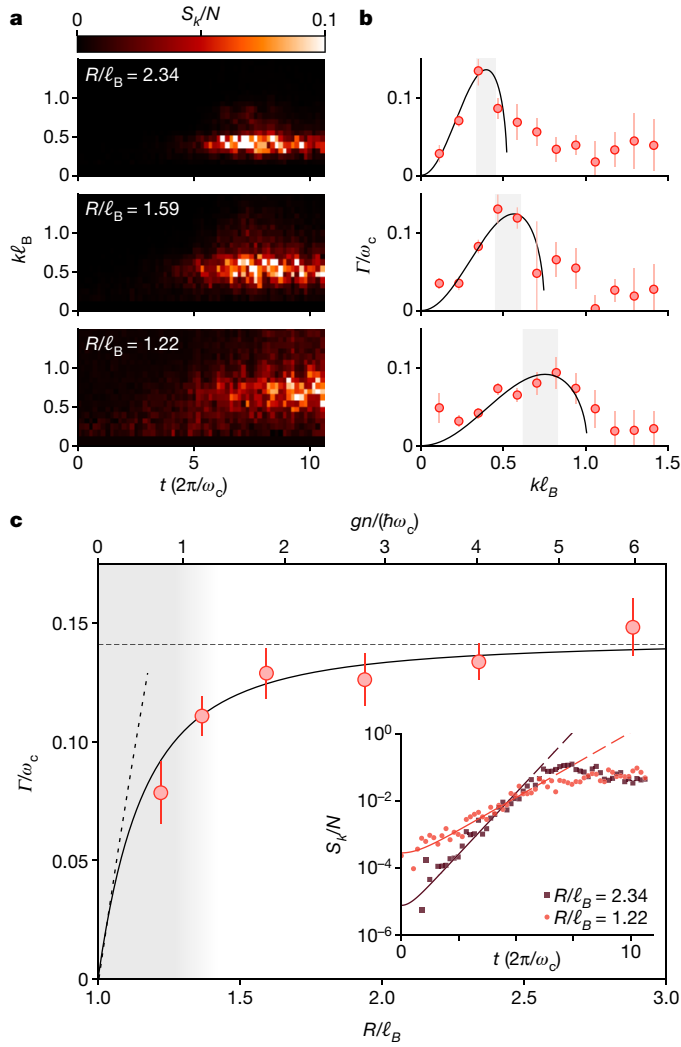


**Fig. 3 | Instability growth dynamics.** **a**, The temporal evolution of the static structure factor,  $S_k(t)$ , for condensates with different initial widths, which reveals a density dependence of both the modulation lengthscale and the growth rate. **b**, The measured instability growth rate,  $\Gamma$ , as a function of wavevector. The solid line shows the rate obtained from our Bogoliubov analysis (see Supplementary Information) and captures the data well with no free parameters. **c**, The instability growth rate at the dominant unstable wavevector shown as a function of the condensate width. The growth rate is obtained by averaging points from the shaded regions in **b**. At high densities we find good agreement with the density-independent hydrodynamic rate  $\Gamma = 0.14\omega_c$  (dashed line). As the density falls, we observe a crossover to the LLL scaling  $\Gamma = 0.21gn/h$  (dotted line). Solid line, Bogoliubov analysis (see Supplementary Information). The inset shows  $S_k(t)$  at  $k_{\max}$  for condensates in the hydrodynamic regime (dark red) and the LLL (light red), along with the corresponding fits used to extract the rate (see text).

approach the LLL prediction  $\Gamma = 0.21gn/h$  indicated by a dotted line. At all densities, the data show good agreement with the rate obtained from our Bogoliubov analysis, reported as the solid line.

After its initial hyperbolic growth,  $S_k$  reaches a steady state, as shown in the inset of Fig. 3c. The emergent crystal is long-lived, with each droplet stabilized by a balance of the outward mean-field pressure and an inwards Coriolis force. This arises from the circulating flow within each droplet which is imposed by the gauge field, and is evident from vortices intersecting adjacent droplets (see Fig. 1e). The counterflow speed at the interface of two droplets of radius  $R$  is  $-\omega_c R$ , giving a gradient of  $m\omega_c R/h$  in the relative phase and a vortex spacing of  $2\pi\ell_B^2/R$ . Adjacent droplets are therefore separated by  $-(R/\ell_B)^2$  vortices. In the limit

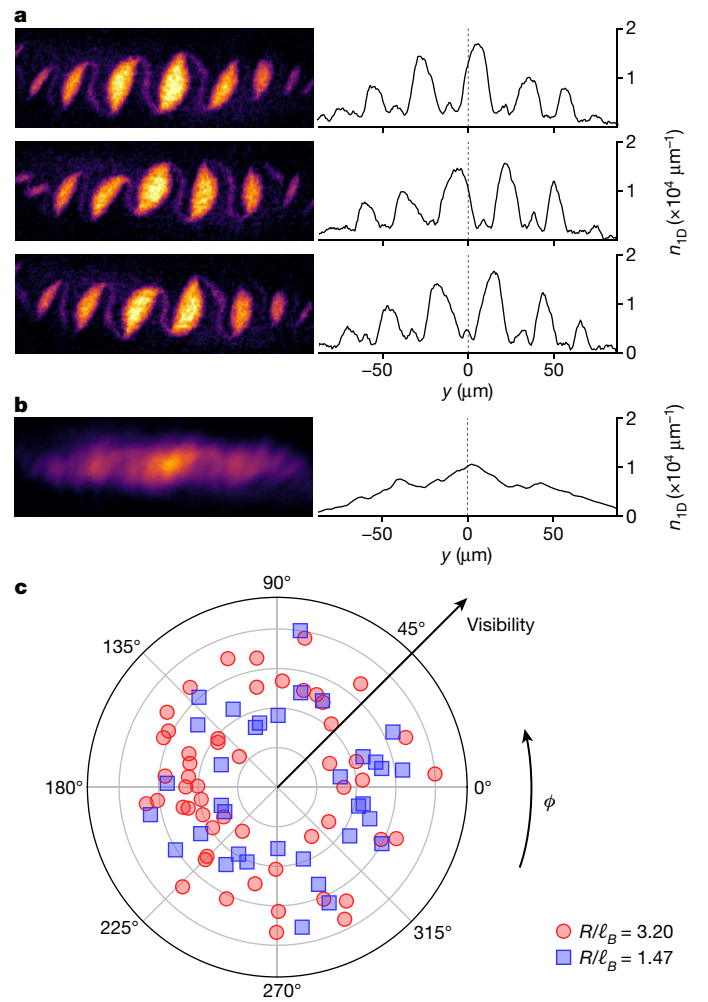


**Fig. 4 | Spontaneous breaking of translational symmetry.** **a**, Images of the emergent crystal in three experimental iterations, along with the integrated one-dimensional density profiles  $n_{1D}(y)$ . The vertical dashed line shows the position of the centre-of-mass of the cloud, relative to which the modulation phase is random. **b**, An image of the cloud averaged over 60 iterations, in which the density modulation is no longer visible. **c**, The phase,  $\phi$ , and visibility of the density modulation measured for multiple iterations of the experiment, for two different initial condensate densities. The visibility appears largely independent of the phase chosen by the modulation. The phase is randomly distributed between 0 and  $2\pi$ , indicating spontaneous breaking of the initial translational symmetry of the cloud.

of classical hydrodynamics this number is large and the quantization of circulation is irrelevant, whereas in the LLL adjacent droplets are separated by a single vortex<sup>15</sup>.

Although the dynamical instability drives the growth of a density modulation, the initial seeding of the unstable mode must arise from thermal or quantum fluctuations in the gas density at  $t = 0$  (see Supplementary Information). Since the phase of these fluctuations is random, this results in spontaneous breaking of the initial translational symmetry of the condensate. In Fig. 4 we show the phase and visibility of the density modulation observed in different iterations of our experiment. To account for small fluctuations in the overall cloud position, we fit the one-dimensional density profile with a sinusoidal function modulated by a Gaussian envelope, and obtain the modulation phase  $\phi$  relative to the centre of mass of the cloud. At all densities we find that the phase is uncorrelated between different experimental realizations, indicating spontaneous breaking of the initial translational symmetry.

The emergent crystallization observed here offers a pristine example of collective physics arising purely from the interplay of interparticle interactions and a gauge field. The steady state breaks both the  $U(1)$  symmetry associated with the phase of the wavefunction and translational symmetry, and thus displays supersolid properties<sup>38</sup>. A natural immediate direction concerns the Goldstone mode associated with the spontaneous breaking of translational symmetry, corresponding to magneto-phonons in the droplet array<sup>9</sup>. This would be a remarkable instance of a propagating mode arising intrinsically from interactions, in the absence of any single-particle dynamics. Although the densities in our experiment correspond to tens of atoms per flux quantum, our protocol can be straightforwardly extended to prepare clouds of lower filling fractions, which are expected to host beyond-mean-field, strongly correlated bosonic quantum Hall states<sup>13–17,19,20,59</sup>.

## Online content

Any methods, additional references, Nature Research reporting summaries, source data, extended data, supplementary information, acknowledgements, peer review information; details of author contributions and competing interests; and statements of data and code availability are available at <https://doi.org/10.1038/s41586-021-04170-2>.

1. Stormer, H. L., Tsui, D. C. & Gossard, A. C. The fractional quantum Hall effect. *Rev. Mod. Phys.* **71**, S298–S305 (1999).
2. Bloch, I., Dalibard, J. & Zwierger, W. Many-body physics with ultracold gases. *Rev. Mod. Phys.* **80**, 885–964 (2008).
3. Cao, Y. et al. Unconventional superconductivity in magic-angle graphene superlattices. *Nature* **556**, 43–50 (2018).
4. Wigner, E. On the interaction of electrons in metals. *Phys. Rev.* **46**, 1002–1011 (1934).
5. Yoshioka, D. & Fukuyama, H. Charge density wave state of two-dimensional electrons in strong magnetic fields. *J. Phys. Soc. Jpn.* **47**, 394–402 (1979).
6. Lam, P. K. & Girvin, S. M. Liquid–solid transition and the fractional quantum-Hall effect. *Phys. Rev. B* **30**, 473–475 (1984).
7. Girvin, S. M., MacDonald, A. H. & Platzman, P. M. Magneto-roton theory of collective excitations in the fractional quantum Hall effect. *Phys. Rev. B* **33**, 2481–2494 (1986).
8. Jiang, H. W. et al. Quantum liquid versus electron solid around  $\nu = 1/5$  Landau-level filling. *Phys. Rev. Lett.* **65**, 633–636 (1990).
9. Jang, J., Hunt, B. M., Pfeiffer, L. N., West, K. W. & Ashoori, R. C. Sharp tunnelling resonance from the vibrations of an electronic Wigner crystal. *Nat. Phys.* **13**, 340–344 (2017).
10. Haldane, F. D. M. & Rezayi, E. H. Finite-size studies of the incompressible state of the fractionally quantized Hall effect and its excitations. *Phys. Rev. Lett.* **54**, 237–240 (1985).
11. Pinczuk, A., Dennis, B. S., Pfeiffer, L. N. & West, K. Observation of collective excitations in the fractional quantum Hall effect. *Phys. Rev. Lett.* **70**, 3983–3986 (1993).
12. Kukulshkin, I. V., Smet, J. H., Scarola, V. W., Umansky, V. & von Klitzing, K. Dispersion of the excitations of fractional quantum Hall states. *Science* **324**, 1044–1047 (2009).
13. Ho, T.-L. Bose–Einstein condensates with large number of vortices. *Phys. Rev. Lett.* **87**, 060403 (2001).
14. Oktel, M. Ö. Vortex lattice of a Bose–Einstein condensate in a rotating anisotropic trap. *Phys. Rev. A* **69**, 023618 (2004).
15. Sinha, S. & Shlyapnikov, G. V. Two-dimensional Bose–Einstein condensate under extreme rotation. *Phys. Rev. Lett.* **94**, 150401 (2005).
16. Cooper, N. R. Rapidly rotating atomic gases. *Adv. Phys.* **57**, 539–616 (2008).
17. Aftalion, A., Blanc, X. & Lerner, N. Fast rotating condensates in an asymmetric harmonic trap. *Phys. Rev. A* **79**, 011603 (2009).
18. Dalibard, J., Gerbier, F., Juzeliūnas, G. & Öhberg, P. Artificial gauge potentials for neutral atoms. *Rev. Mod. Phys.* **83**, 1523–1543 (2011).
19. Chen, X., Gu, Z.-C., Liu, Z.-X. & Wen, X.-G. Symmetry-protected topological orders in interacting bosonic systems. *Science* **338**, 1604–1606 (2012).
20. Senthil, T. & Levin, M. Integer quantum Hall effect for bosons. *Phys. Rev. Lett.* **110**, 046801 (2013).
21. Goldman, N., Juzeliūnas, G., Öhberg, P. & Spielman, I. B. Light-induced gauge fields for ultracold atoms. *Rep. Prog. Phys.* **77**, 126401 (2014).
22. Fletcher, R. J. et al. Geometric squeezing into the lowest Landau level. *Science* **372**, 1318–1322 (2021).
23. Tsui, D. C., Stormer, H. L. & Gossard, A. C. Two-dimensional magnetotransport in the extreme quantum limit. *Phys. Rev. Lett.* **48**, 1559–1562 (1982).
24. Nozières, P. Is the roton in superfluid <sup>4</sup>He the ghost of a Bragg spot? *J. Low Temp. Phys.* **137**, 45–67 (2004).

25. Graß, T. et al. Fractional quantum Hall phases of bosons with tunable interactions: from the Laughlin liquid to a fractional Wigner crystal. *Phys. Rev. Lett.* **121**, 253403 (2018).
26. Galitski, V. & Spielman, I. B. Spin–orbit coupling in quantum gases. *Nature* **494**, 49–54 (2013).
27. Chalopin, T. et al. Probing chiral edge dynamics and bulk topology of a synthetic Hall system. *Nat. Phys.* **16**, 1017–1021 (2020).
28. Struck, J. et al. Tunable gauge potential for neutral and spinless particles in driven optical lattices. *Phys. Rev. Lett.* **108**, 225304 (2012).
29. Jotzu, G. et al. Experimental realization of the topological Haldane model with ultracold fermions. *Nature* **515**, 237–240 (2014).
30. Aidelsburger, M. et al. Measuring the Chern number of Hofstadter bands with ultracold bosonic atoms. *Nat. Phys.* **11**, 162–166 (2015).
31. Stuhl, B. K., Lu, H.-I., Ayccock, L. M., Genkina, D. & Spielman, I. B. Visualizing edge states with an atomic Bose gas in the quantum Hall regime. *Science* **349**, 1514–1518 (2015).
32. Mancini, M. et al. Observation of chiral edge states with neutral fermions in synthetic Hall ribbons. *Science* **349**, 1510–1513 (2015).
33. Schweikhard, V., Coddington, I., Engels, P., Møgelund, V. P. & Cornell, E. A. Rapidly rotating Bose–Einstein condensates in and near the lowest Landau level. *Phys. Rev. Lett.* **92**, 040404 (2004).
34. Bretin, V., Stock, S., Seurin, Y. & Dalibard, J. Fast rotation of a Bose–Einstein condensate. *Phys. Rev. Lett.* **92**, 050403 (2004).
35. Bukov, M., D’Alessio, L. & Polkovnikov, A. Universal high-frequency behavior of periodically driven systems: from dynamical stabilization to Floquet engineering. *Adv. Phys.* **64**, 139–226 (2015).
36. Iordanskii, S. V. & Pitaevskii, L. P. Bose condensation of moving rotons. *Sov. Phys. Usp.* **23**, 317–318 (1980).
37. Pitaevskii, L. P. Layered structure of superfluid <sup>4</sup>He with super-critical motion. *JETP Lett.* **39**, 511–514 (1984).
38. Martone, G. I., Recati, A. & Pavloff, N. Supersolidity of cnoidal waves in an ultracold Bose gas. *Phys. Rev. Res.* **3**, 013143 (2021).
39. Mottl, R. et al. Roton-type mode softening in a quantum gas with cavity-mediated long-range interactions. *Science* **336**, 1570–1573 (2012).
40. Léonard, J., Morales, A., Zupancic, P., Esslinger, T. & Donner, T. Supersolid formation in a quantum gas breaking a continuous translational symmetry. *Nature* **543**, 87–90 (2017).
41. Ji, S.-C. et al. Softening of roton and phonon modes in a Bose–Einstein condensate with spin–orbit coupling. *Phys. Rev. Lett.* **114**, 105301 (2015).
42. Li, J.-R. et al. A stripe phase with supersolid properties in spin–orbit-coupled Bose–Einstein condensates. *Nature* **543**, 91–94 (2017).
43. Ha, L.-C., Clark, L. W., Parker, C. V., Anderson, B. M. & Chin, C. Roton–maxon excitation spectrum of Bose condensates in a shaken optical lattice. *Phys. Rev. Lett.* **114**, 055301 (2015).
44. Feng, L., Clark, L. W., Gaj, A. & Chin, C. Coherent inflationary dynamics for Bose–Einstein condensates crossing a quantum critical point. *Nat. Phys.* **14**, 269–272 (2018).
45. Zhang, Z., Yao, K.-X., Feng, L., Hu, J. & Chin, C. Pattern formation in a driven Bose–Einstein condensate. *Nat. Phys.* **16**, 652–656 (2020).
46. Petter, D. et al. Probing the roton excitation spectrum of a stable dipolar Bose gas. *Phys. Rev. Lett.* **122**, 183401 (2019).
47. Hertkorn, J. et al. Density fluctuations across the superfluid–supersolid phase transition in a dipolar quantum gas. *Phys. Rev. X* **11**, 011037 (2021).
48. Schmidt, J.-N. et al. Roton excitations in an oblate dipolar quantum gas. *Phys. Rev. Lett.* **126**, 193002 (2021).
49. Guo, M. et al. The low-energy Goldstone mode in a trapped dipolar supersolid. *Nature* **574**, 386–389 (2019).
50. Tanzi, L. et al. Supersolid symmetry breaking from compressional oscillations in a dipolar quantum gas. *Nature* **574**, 382–385 (2019).
51. Chomaz, L. et al. Long-lived and transient supersolid behaviors in dipolar quantum gases. *Phys. Rev. X* **9**, 21012 (2019).
52. Davidson, R. C., Chan, H.-W., Chen, C. & Lund, S. Equilibrium and stability properties of intense non-neutral electron flow. *Rev. Mod. Phys.* **63**, 341–374 (1991).
53. Cerfon, A. J. Vortex dynamics and shear-layer instability in high-intensity cyclotrons. *Phys. Rev. Lett.* **116**, 174801 (2016).
54. Chandrasekhar, S. C. *Hydrodynamic and Hydromagnetic Stability* (Clarendon Press, 1961).
55. Landau, L. D. & Lifshitz, E. M. *Fluid Mechanics* (Pergamon Press, 1987).
56. Finne, A. P. et al. Dynamics of vortices and interfaces in superfluid <sup>3</sup>He. *Rep. Prog. Phys.* **69**, 3157–3230 (2006).
57. Baggaley, A. W. & Parker, N. G. Kelvin–Helmholtz instability in a single-component atomic superfluid. *Phys. Rev. A* **97**, 053608 (2018).
58. Fetter, A. L. & Walecka, J. D. *Quantum Theory of Many-particle Systems* (McGraw-Hill, 1971).
59. Recati, A., Zambelli, F. & Stringari, S. Overcritical rotation of a trapped Bose–Einstein condensate. *Phys. Rev. Lett.* **86**, 377–380 (2001).

**Publisher’s note** Springer Nature remains neutral with regard to jurisdictional claims in published maps and institutional affiliations.

© The Author(s), under exclusive licence to Springer Nature Limited 2022

## Methods

### Preparation of Landau gauge condensates

We prepare condensates occupying a single Landau gauge wavefunction using the geometric squeezing protocol described in ref. <sup>22</sup>. We begin with a condensate of  $8.1(1) \times 10^5$  atoms of  $^{23}\text{Na}$  in an elliptical time-orbiting-potential (TOP) trap<sup>60</sup>, with an root-mean-square (r.m.s.) radial frequency  $\omega = 2\pi \times 88.6(1)$  Hz, ellipticity 0.125(4), and axial frequency  $2.8\omega$ . We then rotate the ellipticity of the trap, ramping the rotation frequency from zero to  $\omega$ . In the rotating frame, atoms experience both a synthetic magnetic field and a scalar saddle potential. Isopotential flow on this saddle, in analogy to the  $\mathbf{E} \times \mathbf{B}$  Hall drift of electromagnetism, leads to elongation and contraction of the condensate along orthogonal directions and effecting unitary squeezing of the atomic density distribution<sup>22</sup>. We then turn off the saddle potential by setting the trap ellipticity to zero, which halts the outward flow of atoms. This results in an equilibrium, quasi-translationally invariant condensate freely rotating at  $\omega$ , which we allow to evolve for a variable time  $t$ . Finally, we obtain an absorption image of the in situ density distribution.

### Imaging setup

Our imaging resolution is sufficient to observe vortices in situ with a contrast of  $\sim 60\%$  (ref. <sup>22</sup>). In the Thomas–Fermi regime, these have a characteristic size set by the healing length, which is  $\sim 300$  nm in our system. This is substantially smaller than the quantum mechanical ground state size of cyclotron orbits, set by the rotational analogue of the magnetic length,  $\ell_B = \sqrt{\hbar/(2m\omega)} = 1.6 \mu\text{m}$ .

### Coupling constant

Given interaction energies close to the LLL, the axial motion at frequency  $2.8\omega$  is predominantly in its ground state. The coupling constant is then  $g = \frac{4\pi\hbar^2 a}{m} \int dz |\phi(z)|^4$ , where  $a$  is the three-dimensional  $s$ -wave scattering length,  $m$  denotes the atomic mass of  $^{23}\text{Na}$  and  $\phi(z)$  is the axial wavefunction with normalization  $\int dz |\phi(z)|^2 = 1$ .

### Stability analysis

To theoretically investigate the crystallization process, we perform a stability analysis of the initial Landau gauge condensate. In the Thomas–Fermi limit, we may neglect the quantum pressure term in the superfluid hydrodynamic equations. We linearize the equations about the original unperturbed condensate<sup>61</sup>, and find an exact analytical solution for the density and the velocity perturbations in terms of the Heun function<sup>62</sup>. The initial counterflow leads to an instability of Kelvin–Helmholtz type, and the analysis displays a dynamical instability with a most critical wavevector at  $k_{\text{max}} = 1.12/R_{\text{TF}} = 0.95/R$  and a rate  $\Gamma = 0.14\omega_c$ . To treat the entire region from the LLL to the Thomas–Fermi regime, we perform a numerical Bogoliubov analysis. In the LLL limit, the crystallization growth rate is given by  $\Gamma = 0.21gn/\hbar$ , and the most critical wavevector is  $k_{\text{max}} \rightarrow 0.981/\ell_B$ . The Bogoliubov analysis shows that the growth rate of the dominant wavevector evolves smoothly from being interaction-dominated ( $\Gamma \approx 0.21gn/\hbar$ ) in the LLL regime, to being set by the cyclotron frequency ( $\Gamma \approx \omega_c$ ) in the Thomas–Fermi regime. Further details are provided in the Supplementary Information.

### Gross–Pitaevskii simulation

To provide insight into the crystallization dynamics beyond what can be captured in the linear stability analysis, we perform a numerical simulation of our experiment based upon the Gross–Pitaevskii (GP) equation. Within a single-mode approximation, the condensate wavefunction  $\psi(r, t)$  evolves in the rotating frame as

$$i\hbar \frac{\partial}{\partial t} \psi = \left[ \frac{-\hbar^2 \nabla^2}{2m} + V + g|\psi|^2 - \mathbf{\Omega} \cdot \mathbf{L} \right] \psi. \quad (4)$$

Here  $g = \sqrt{8\pi} \frac{\hbar^2 a_s}{m l_z}$  is the two-dimensional mean-field coupling constant,  $a_s = 3.3$  nm is the scattering length,  $l_z = \sqrt{\frac{\hbar}{m\omega_z}}$  is the harmonic oscillator length of the axial trap,  $\omega_z = 2.8\omega$  is the trap frequency in the  $z$ -direction,  $\omega = 2\pi \times 88.6$  Hz is the r.m.s. radial trap frequency,  $\mathbf{\Omega} = \mathbf{\Omega}(t)\hat{z}$  is the angular velocity,  $\mathbf{L}$  is the angular momentum operator, and  $V$  is a complex scalar potential. The real part  $\text{Re}(V) = \frac{1}{2}m\omega^2[(1+\varepsilon)x^2 + (1-\varepsilon)y^2]$  is the radial trapping potential with ellipticity  $\varepsilon$ , and the imaginary part  $\text{Im}(V) \propto 1 + \text{erf}[(r - R_\infty)/\sigma]$  serves as an absorbing circular boundary. The absorbing radius  $R_\infty$  is chosen to be much larger than the transverse size of the condensate, and we use a wall thickness  $\sigma = R_\infty/10$ . We implement the evolution of equation (4) on a square grid using the time-splitting spectral method<sup>63</sup> and accelerate the simulation by performing the bulk of the computation on a graphics processing unit (GPU).

The simulated experimental sequence is identical to the experiment. We first perform geometric squeezing of an initially circular condensate<sup>22</sup>, before setting the trap ellipticity  $\varepsilon \rightarrow 0$  after which the condensate evolves freely for a time  $t$  in the rotating frame.

We find that without the explicit addition of noise, the condensate does not exhibit any instability except near the boundaries, owing to residual edge effects not mitigated by the absorbing potential (see Extended Data Fig. 1a). On the other hand, seeding of the dynamical instability by the addition of Gaussian phase noise at time  $t = 0$  results in a very similar simulated evolution (Extended Data Fig. 1b) compared to the experiment (Extended Data Fig. 1c).

We perform an identical analysis procedure as in the experiment (see main text) on the simulated density profiles in order to obtain the structure factor  $S_k(t)$ , shown in Extended Data Fig. 1d, e, and the instability growth rate shown in Extended Data Fig. 1f. The red points show the experimental instability growth rate as a function of wavevector  $k$ , and the black line shows the prediction of our Bogoliubov analysis. For comparison, the blue line shows the rate extracted from the simulation, which captures the observed growth at higher wavevectors than the unstable range predicted by the Bogoliubov approach. This suggests that such growth can indeed be attributed to nonlinear effects, which are not captured by the perturbative Bogoliubov approach. In addition to oscillations in  $S_k$  at the cyclotron frequency  $\omega_c$ , a slower modulation is also observed. We attribute this oscillation to rotation of the individual droplets in the crystal.

In both experiment and simulation the emergent crystal is long-lived, persisting for  $\omega_c t/(2\pi) > 20$ . In the experiment the lifetime is only limited by the weak  $\propto r^4$  anharmonicities in the trapping potential, leading to a slow S-shaped distortion of the linear crystal, similar to the Kerr effect on nonclassical states in quantum optics.

### Vortex detection and phase profile

In the rotating frame, each droplet exhibits an irrotational flow profile, with vortices surrounding the droplets. These vortices are directly visible in the experimental density image, and can be used to reconstruct the phase profile of the crystal in the rotating frame (see Extended Data Fig. 2a, c, e). The phase is determined by the locations of the vortices, which are assumed to each have a single unit of circulation  $2\pi\hbar/m$ . Most vortices are outside of the bulk of the condensate, making their detection challenging. Nevertheless, a numerical solution of the GP equation shows similarly located vortices (Extended Data Fig. 2d), as well as a similar irrotational flow profile in the rotating frame (Extended Data Fig. 2f).

### Data availability

All data files are available from the corresponding author upon request. Accompanying data, including those for figures, are available from Zenodo (<https://doi.org/10.5281/zenodo.5533142>).

## Code availability

The simulation and analysis code are available from the corresponding author upon reasonable request.

60. Petrich, W., Anderson, M. H., Ensher, J. R. & Cornell, E. A. Stable, tightly confining magnetic trap for evaporative cooling of neutral atoms. *Phys. Rev. Lett.* **74**, 3352–3355 (1995).
61. Sinha, S. & Castin, Y. Dynamic instability of a rotating Bose–Einstein condensate. *Phys. Rev. Lett.* **87**, 190402 (2001).
62. Ronveaux, A. (ed.) *Heun's Differential Equations* (Oxford Univ. Press, 1995).
63. Bao, W. & Wang, H. An efficient and spectrally accurate numerical method for computing dynamics of rotating Bose–Einstein condensates. *J. Comput. Phys.* **217**, 612–626 (2006).

**Acknowledgements** We thank T. Pfau and his research group, J. Dunkel, A. Fetter, T. Senthil, T. Simula and W. Zwerger for discussions. This work was supported by the National Science Foundation (Center for Ultracold Atoms and grant no. PHY-2012110), Air Force Office of Scientific Research (FA9550-16-1-0324 and MURI Quantum Phases of Matter FA9550-14-1-

0035), Office of Naval Research (N00014-17-1-2257), the DARPA A-Phi program through ARO grant W911NF-19-1-0511, and the Vannevar Bush Faculty Fellowship. A.S. acknowledges support from the NSF GRFP. M.Z. acknowledges funding from the Alexander von Humboldt Foundation.

**Author contributions** B.M., A.S., C.C.W., P.B.P., Z.Y. and R.J.F. constructed the apparatus. B.M., A.S., C.C.W. and R.J.F. performed the measurements. B.M. and A.S. analysed the data. B.M. contributed the GP numerical simulations. V.C., R.J.F. and M.Z. developed the theoretical description. R.J.F. and M.Z. supervised the project. All authors contributed to interpretation of the results and preparation of the manuscript.

**Competing interests** The authors declare no competing interests.

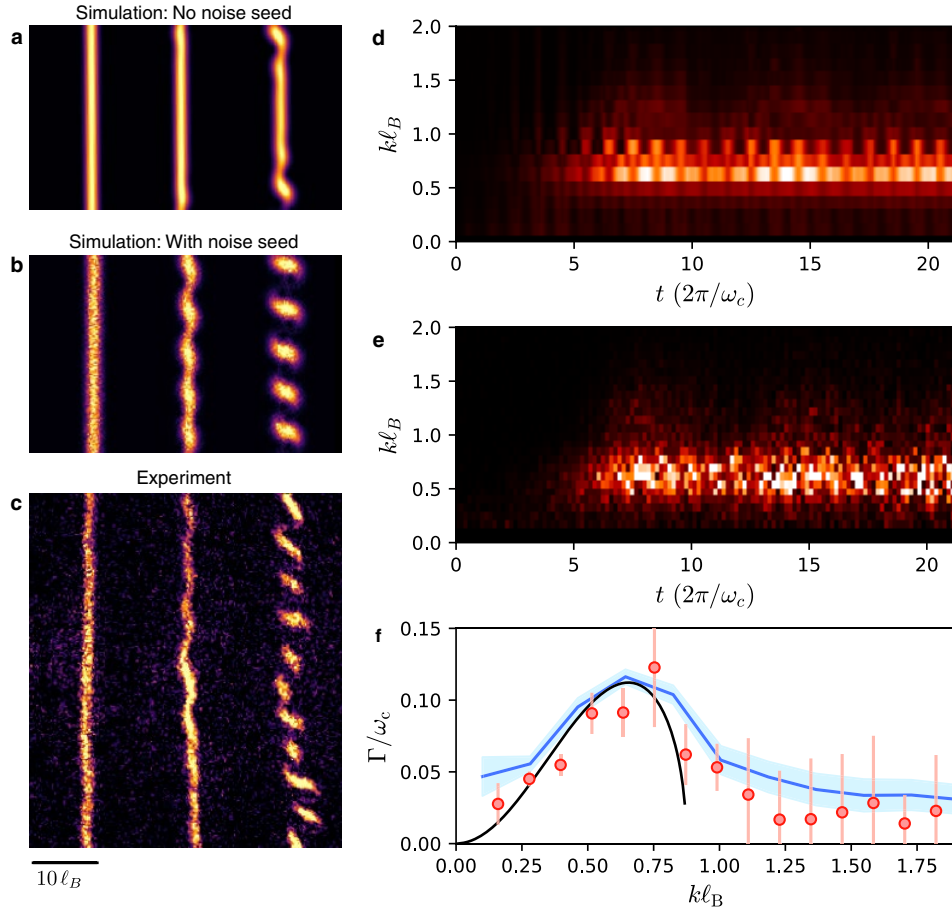
## Additional information

**Supplementary information** The online version contains supplementary material available at <https://doi.org/10.1038/s41586-021-04170-2>.

**Correspondence and requests for materials** should be addressed to Martin Zwierlein.

**Peer review information** *Nature* thanks Alessio Recati and the other, anonymous, reviewer(s) for their contribution to the peer review of this work.

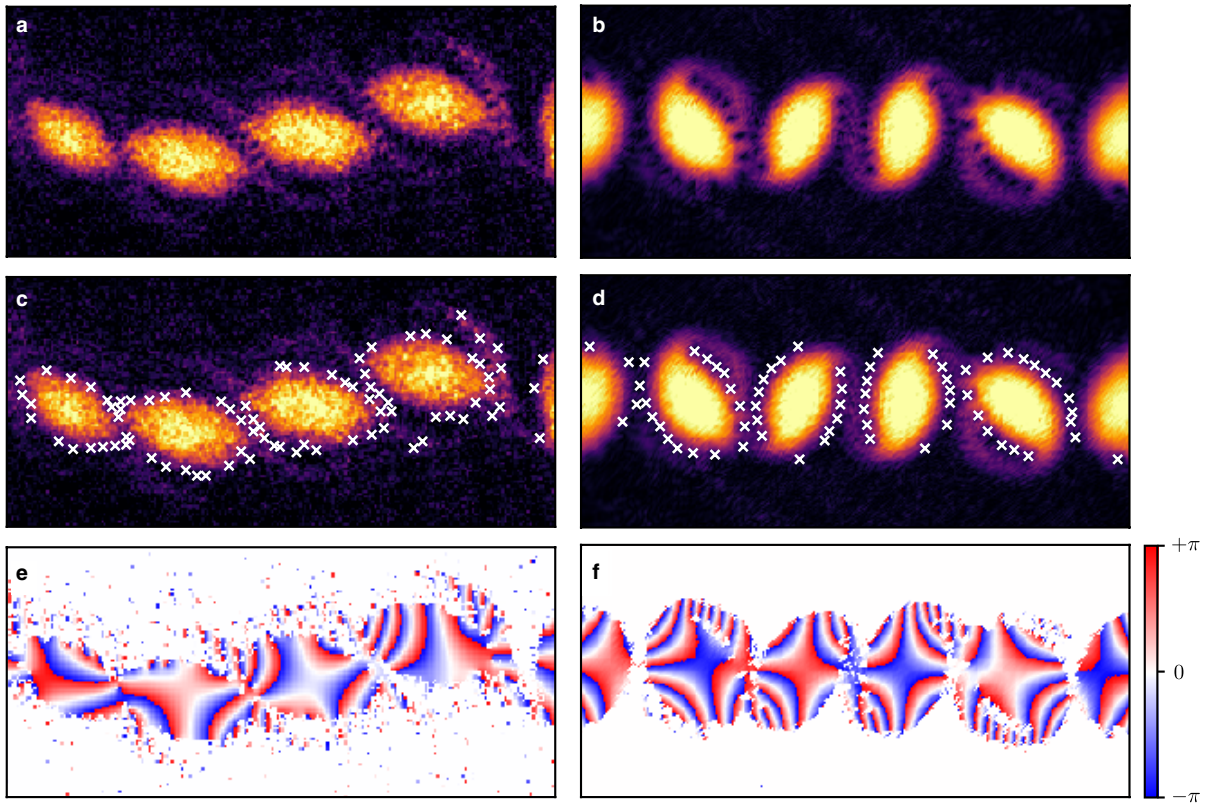
**Reprints and permissions information** is available at <http://www.nature.com/reprints>.



**Extended Data Fig. 1 | Numerical GP simulation of the condensate evolution in the rotating frame. a–c,** Time evolution of the condensate density without the addition of noise (top), with added phase noise (middle), and in the experiment (bottom). The frames correspond to times  $\omega_c t/(2\pi) = 0, 4$  and  $6$ . **d–e,** Evolution of the structure factor  $S_k(t)$  extracted from the simulation (d) and the experiment (e) which show good agreement. **f,** The extracted

instability growth rate as a function of wavevector  $k$ . The experimental measurements are shown by red points, and the Bogoliubov prediction by the black line. The blue line shows the result of the GP simulation. Here, the blue shading and the red error bars indicate  $1\sigma$  standard error. This model captures the experimentally measured growth at wavevectors above the instability region provided by the linear Bogoliubov description.





**Extended Data Fig. 2 | Phase profile of the crystal.** **a, b**, The density profiles of the crystals in the experiment (**a**) and GP simulation (**b**) appear to contain vortices, which are marked in **c** and **d**. **e**, The phase of the macroscopic wavefunction can be inferred from the locations of the vortices in the

experimental image. Note that additional contributions from undetected vortices may exist. **f**, The simulated phase profile from a GP simulation shows a similar structure of irrotational flow within each segment of the crystal. In both **e** and **f**, the phase shown is in the rotating frame.